INVERSE DYNAMIC MODELLING
OF A PARALLEL ROBOTIC SYSTEM FOR BRACHYTHERAPY

Nicolae PLITEA, Bogdan GHERMAN, Dragos COCOREAN, Calin VAIDA, Doina PISLA

Research Center for Industrial Robots Simulation and Testing, Technical University of Cluj-Napoca, Romania
Corresponding authors: Bogdan Gherman, E-mail: `bogdan.gherman@mep.utcluj.ro,`

Abstract. Robotic assisted brachytherapy is a dynamic field of research due to its tangible and immediate results in the improvement of cancer patient's life conditions. The inverse dynamic model of a parallel robotic system for general brachytherapy is presented in this paper. The PARA-BRACHYROB robotic system has 5 degrees of freedom (DOF), five for position and orientation of the needle insertion module plus a redundant DOF dedicated for needle insertion. The dynamic model is obtained using the virtual work method and the dynamically equivalent lumped masses of the experimental model. A validation of the numerical results using a multi-body simulation software (the Siemens NX RecurDyn) is also presented, proving the accuracy of the developed model.

Key words: workspace, singularities, parallel robot, accuracy, needle placement.

1. INTRODUCTION

Nowadays the world encounters a very provocative challenge: the number of cancer patients is constantly increasing, the most affected organs being the colon, lungs, prostate and bowel. Brachytherapy (BT) is a relatively new approach in the fight against cancer, implying the irradiation of the tumor only, by placing inside of it several radiation seeds using a required number of catheters. Many researchers proposed solutions, most of them for prostate cancer treatment: [0, 2].

For an efficient and robust control of the needle trajectory, in order to avoid any deflection, the use and implementation of the dynamic model of the robot becomes a necessity. Strasmann, in [0] proposes a thorough study to estimate the dynamic characteristics of the needle insertion stage, while Sadjadi shows in [0] the needle deflection error spread for different targeted depths. In [0, 5, 6] the authors use the Newton-Euler approach has been used to calculate the actuation and reaction forces of the mechanism. The Lagrange formalism introduces scalar multipliers for each kinematic closure equation. Abdellatif [0] in as well as Miller and Clavel in [0] used the Lagrangian formalism for closed-loop mechanisms (although reputed of being inefficient). The virtual work ([0, 10, 11, 12]) formulation is considered as a mixed form of all above mentioned methods and is far more efficient because it can eliminate all forces and internal joints and it allows direct determination of forces/torques of the robot. Staicu in [0] and [0] developed the inverse kinematic and dynamic model of an orienting gear train mechanism using recursive matrix relations. Section 2 of the paper is dedicated to the description of the studied parallel robot for BT and the analytic inverse dynamic model. Section 3 presents the simulation dynamics results, showing the validation of the inverse dynamics using the Siemens NX solver software. The conclusions are presented at the end of the paper.

2. INVERSE DYNAMICS OF THE PARA-BRACHYROB PARALLEL ROBOT

PARA-BRACHYROB is a parallel robot that has 5-DOF and two modules: the first one has 3-DOF and 3 active joints, namely: q_1, q_2, q_3 while the second one has 3-DOF and 2 active joints, namely: q_4, q_5 (Fig. 1). Each module works in cylindrical coordinates. The coordinates q_1, q_2, q_4, q_5 are prismatic joints along an axis parallel with OZ, while the third motion of each module is a rotation around the same axis,

with the first rotation joint, q_3 as an active joint, while the second rotation joint (for the second module) is a passive joint. Besides the active coordinates q_1, q_2, q_3, q_4, q_5 the PARA-BRACHYROB parallel robot for BT has an additional, redundant 1-DOF mechanism represented by the q_6 active joint, used only for the needle insertion. The kinematic model of the robot has been presented in detail in [0], the only difference consisting in the additional 1 DOF needle insertion module, [0, 15].

The inverse dynamic model of the PARA-BRACHYROB experimental model (Fig. 2) has been developed using the virtual work principle. The input data for inverse dynamics consist in: the motion laws of the robot for posing (position and orientation of the end-effector), the inverse kinematic model (positions, velocities and accelerations) and the masses of robot elements. Applying the algorithm equations for inverse dynamics, the drive forces and torques will be obtained. Applying the virtual work principle, the torque vector is obtained: $\tau = [F_1, F_2, M_3, F_4, F_5, F_6]^T$ where F_1, F_2, F_4, F_5, F_6 are the linear forces obtained at the level of each active corresponding joint and M_3 is the torque in the q_3 active rotational joint (Fig. 1).

For the determination of the inverse dynamic model, the following moving elements of the robot structure have been considered (Fig. 3): the elements (1) $\div$ (28), having the masses $m_1 \div m_{28}$; the ball screws (29), (30), (31), (32), all the same having the mass m_{29}; the speed reducers (33), (34), (36), (37) for the q_1, q_2, q_4, q_5 active joints, having the masses m_{33}, the speed reducer (35) for the q_3 active joint, having the mass m_{34}; the couplings, all identical, having the masses: m_{35}; the motors (38), (39), (40), (41), (42), all identical, having the mass: m_{36}, the motor (43) corresponding to the q_6 active joint, with the mass m_{37} with the speed reducer (44) having the mass m_{38}; the pulleys (45) corresponding to the q_6 active joint, each with the mass m_{39}, the screw (46) corresponding to the q_6 active joint, with the mass m_{40}. The following lengths have been considered, measured on Z axis: $l_1 \div l_8$ and $l_{10} \div l_{14}$, while l_9 has been measured along the needle axis.

Two simplifying hypotheses have been used to develop the dynamic model: the use of lumped masses and the neglecting of friction forces. In order to use the masses of the moving bodies in the robot dynamic equations, a simple way is to concentrate these masses into one or several key-points. Thus, a bar having the length l and mass m is dynamic equivalent to the three points (two of equal mass, at the two ends of the bar: $m_A = m_B = 1/6m$) and the other one in the middle: $m_C = 2/3m$ [0].

For the spline shaft, the moment of inertia I_1 was computed using (1), where D_{28} represents the spline shaft diameter ($D_{28} = D_{29} = 25$mm). The inertia moment of the bodies that rotate around the Z axis of the robot (the spline shaft (28)) has been taken from the CAD model (I_2 and I_3), the same being applied for the bodies that rotate around the fixed cylindrical shaft (47): I_4 and I_5. The inertia moment of the ball screws (29–32), can be determined in using (2), where D_{29} represents the nominal diameter of the ball screws. Knowing the inertia moment of the motors (38), (39), (40), (41), (42) as being I_7, of the speed reducers (33), (34), (36), (37) as being I_8, of the speed reducer (35) as I_9 and of the couplings as I_{10} and using the kinetic energy as in (2), the reduced moment to the active joint q_3 and respectively to the fixed cylinder shaft (47) is obtained using (3-4), where $n_2 = 236$ is the gear ratio of the speed reduction unit (35).

$$I_1 = m_{28} \cdot D_{28}^2 / 8 \quad [\text{kg} \cdot \text{mm}^2] \tag{1}$$

$$I_6 = m_{29} \cdot D_{29}^2 / 8 \quad [\text{kg} \cdot \text{mm}^2] \tag{2}$$

$$E = \tfrac{1}{2} m_{red} \cdot v^2 + \tfrac{1}{2} I_{red} \cdot \omega^2 \; ; \quad E_{cyl} \equiv \tfrac{1}{2} I_{red\_cyl} \cdot \dot{\alpha}^2 = \frac{1}{2}(I_3 + I_4) \cdot \dot{\alpha}^2 \tag{3}$$

$$E_{q3} \equiv I_{red\_q3} \cdot \dot{q}_3^2 / 2 = (I_1 + I_9 + I_{10} + I_2 + I_3) \cdot \dot{q}_3^2 / 2 + I_7 \cdot (\dot{q}_3 \cdot n_2)^2 / 2 \tag{4}$$

The expressions of the reduced inertia moments to the speed reducer (<u>35</u>), respectively the mass center of the fixed cylindrical shaft (<u>47</u>) are:

$$I_{red\_q_3} = I_1 + I_9 + I_{10} + I_2 + I_3 + I_7 \cdot n_2^2 \,; \quad I_{red\_cyl} = I_3 + I_4 \tag{5}$$
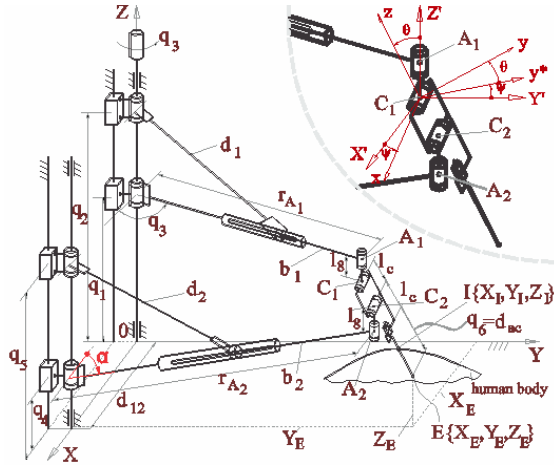

Fig. 1 – The kinematic scheme of PARA-BRACHYROB parallel robot for brachytherapy.
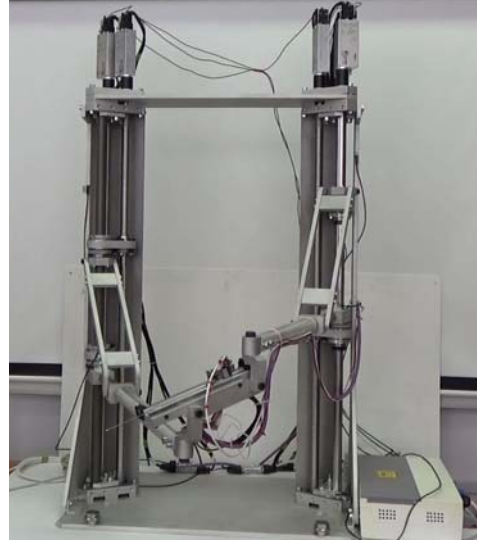
Fig. 2 – The experimental model of PARA-BRACHYROB parallel robot for brachytherapy.

The gyration radius has been computed, both for the q_3 active joint as well as for the cylindrical shaft (<u>47</u>):

$$i_{\Delta 30} = \sqrt{I_{red\_q_3} / \left(m_{28} + m_{34} + m_{35} + m_{36} + m_2 + m_3 + m_5 + m_6 + \left(m_7 + m_{10}\right)/6\right)} \quad [\text{mm}] \tag{6}$$

$$i_{\Delta 31} = \sqrt{I_{red\_cyl} / \left(m_{12} + m_{13} + m_{15} + m_{16} + \left(m_{17} + m_{18}\right)/6\right)} \quad [\text{mm}]. \tag{7}$$

For the active joint q_6, the inertia moment of the motor (<u>43</u>) (I_{11}) and speed reducer (<u>44</u>) (I_{12}) have been taken from the producer's catalogue and the inertia moment of the pulleys (<u>45</u>) and screw (<u>46</u>) have been computed in (8).

$$I_{13} = m_{39} \cdot D_{45}^2 / 8 \ [\text{kg} \cdot \text{mm}^2]; \ I_{14} = m_{40} \cdot D_{46}^2 / 8 \ [\text{kg} \cdot \text{mm}^2]. \tag{8}$$

The reduced inertia moment to the speed reducers shafts has been computed in (9) and the subsequent gyration radii in (10).

$$I_{red\_i} \cdot \left(\dot{q}_i^* / 2\right)^2 / 2 = I_7 \cdot \left(\dot{q}_i^* \cdot n_1\right)^2 / 2 + \left(\dot{q}_i^*\right)^2 / 2 \cdot \left(I_6 + I_8 + I_{10}\right) = I_7 \cdot n_1^2 + I_6 + I_8 + I_{10}; \ i = 1, 2, 4, 5 \tag{9}$$

$$i_{\Delta 32} = \sqrt{I_{red\_i} / \left(m_{29} + m_{33} + m_{35} + m_{36}\right)} \quad [\text{mm}], \tag{10}$$

with $i_{\Delta 33} = i_{\Delta 34} = i_{\Delta 35} = i_{\Delta 32}$. The reduced inertia moment to the motor (<u>43</u>) has been computed in (11) and the gyration radius in (12). q_i^* is computed using (13) where q_{i0} represents the position of the active joints q_1, q_2, q_4, q_5 at the beginning of motion, *P* is the screw lead (*P* = 5 mm), while for q_6^*, *p* = 0.8 mm.

$$I_{red\_6} = I_{11} \cdot n_3^2 + I_{12} + 2 \cdot I_{13} + I_{14}, \tag{11}$$

$$i_{\Delta 36} = \sqrt{I_{red\_6} / \left(m_{37} + m_{38} + 2 \cdot m_{39} + m_{40}\right)} \quad [\text{mm}], \tag{12}$$

$$q_i^* = 2\pi / P \cdot (q_i - q_{i0}), \ i = 1,2,4,5; \quad q_6^* = 2\pi / P \cdot (q_6 - q_{60}). \tag{13}$$

Starting from these masses, a number of 43 lumped masses (14) are considered as input data into the inverse dynamics algorithm, as presented in Fig. 4.

The following notations have been used for the inverse dynamic model: $q = [q_1, q_2, q_3, q_4, q_5, q_6]^T$, $\dot{q} = [\dot{q}_1, \dot{q}_2, \dot{q}_3, \dot{q}_4, \dot{q}_5, \dot{q}_6]^T$, $\ddot{q} = [\ddot{q}_1, \ddot{q}_2, \ddot{q}_3, \ddot{q}_4, \ddot{q}_5, \ddot{q}_6]^T$ – the vector of the active joint coordinates; speeds, respectively accelerations; $\delta q = [\delta q_1, \delta q_2, \delta q_3, \delta q_4, \delta q_5, \delta q_6]^T$ – the vector of virtual displacements for the active joint positions; $X_P = [X_E, Y_E, Z_E]^T$, $\dot{X}_P = [\dot{X}_E, \dot{Y}_E, \dot{Z}_E]^T$, $\ddot{X}_P = [\ddot{X}_E, \ddot{Y}_E, \ddot{Z}_E]^T$ – the vector of the E point coordinates, velocities and accelerations; $\delta X_P = [\delta X_E, \delta Y_E, \delta Z_E]^T$ - the vector of virtual displacements of the E point coordinates; $X_{Mi} = [X_i, Y_i, Z_i]^T$, $\dot{X}_{M_i} = [\dot{X}_i, \dot{Y}_i, \dot{Z}_i]^T$, $\ddot{X}_{M_i} = [\ddot{X}_i, \ddot{Y}_i, \ddot{Z}_i]^T$ – the vectors of the mass coordinates in m_i^* equivalent points with the system with 47 mobile bodies of the robot, velocities and accelerations; $\delta X_{M_i} = [\delta X_i, \delta Y_i, \delta Z_i]^T$ – the vector of virtual displacements of the m_i^* points coordinates; $\tau = [\tau_1, \tau_2, \tau_3, \tau_4, \tau_5, \tau_6]^T = [F_1, F_2, M_3, F_4, F_5, F_6]^T$ – the vector of active forces/moments;

$$m_{Mass\_i} = \begin{bmatrix} m_i^* & 0 & 0 \\ 0 & m_i^* & 0 \\ 0 & 0 & m_i^* \end{bmatrix}; \ G = \begin{bmatrix} 0 \\ 0 \\ -g \end{bmatrix} - \text{the gravitational acceleration vector, } i = 1, 2, \ldots, 43.$$
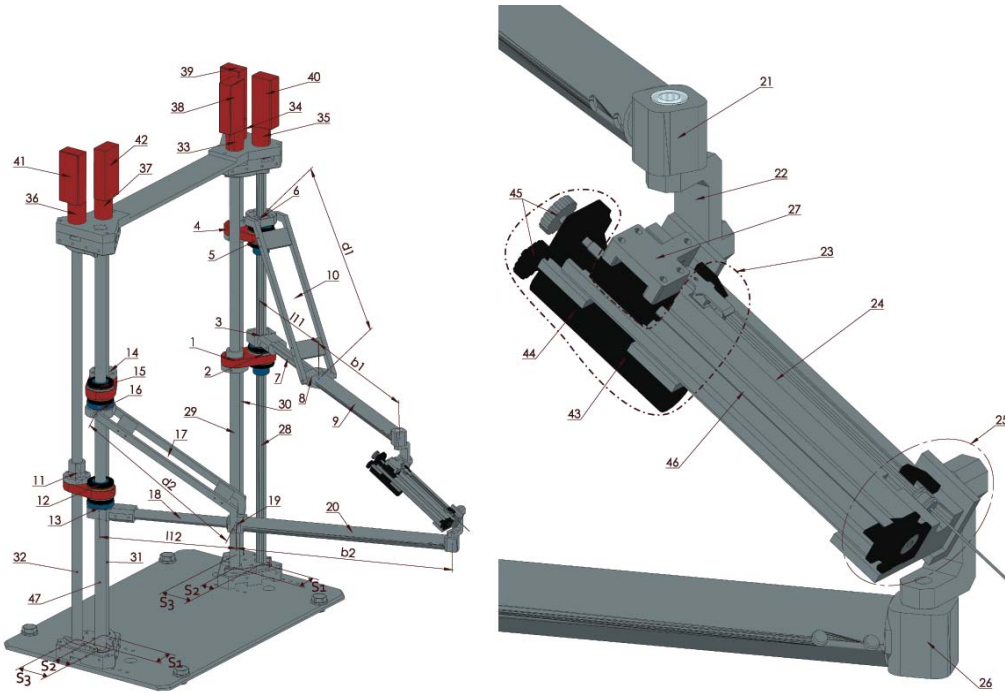

Fig. 3 – The CAD model of PARA-BRACHYROB parallel robot.

$$m_1^* = m_1; \ m_2^* = m_2; \ m_3^* = m_3 + m_7 / 6; \ m_4^* = m_4; \ m_5^* = m_5; \ m_6^* = m_6 + m_{10} / 6; \ m_7^* = 2m_7 / 3; \ m_8^* = m_7 / 6;$$

$$m_9^* = m_8 + m_9 / 6 + m_{10} / 6; \ m_{10}^* = 2m_9 / 3; \ m_{11}^* = m_{21} + m_9 / 6; \ m_{12}^* = 2m_{10} / 3; \ m_{13}^* = m_{11}; \ m_{14}^* = m_{12};$$

$$m_{15}^* = m_{13} + m_{18} / 6; \ m_{16}^* = m_{14}; \ m_{17}^* = m_{15}; \ m_{18}^* = m_{16} + m_{17} / 6; \ m_{19}^* = 2m_{18} / 3; \ m_{20}^* = m_{18} / 6;$$

$$m_{21}^* = m_{19} + m_{17} / 6 + m_{20} / 6; \ m_{22}^* = 2m_{20} / 3; \ m_{23}^* = m_{26} + m_{20} / 6; \ m_{24}^* = 2m_{17} / 3; \ m_{25}^* = m_{22};$$

$$\tag{14}$$

$$m_{26}^* = m_{23} + m_{24}/6; \quad m_{27}^* = 2m_{24}; \quad m_{28}^* = m_{25} + m_{24}/6; \quad m_{29}^* = m_{27};$$

$$m_{30}^* = m_{31}^* = \left[m_{28} + m_{34} + m_{35} + m_{36} + m_2 + m_3 + m_5 + m_6 + (m_7 + m_{10})/6 \right]/2;$$

$$m_{32}^* = m_{33}^* = \left[m_{12} + m_{13} + m_{15} + m_{16} + (m_{17} + m_{18})/6 \right]/2; \quad m_{34}^* = m_{35}^* = m_{36}^* = m_{37}^* = (m_{29} + m_{33} + m_{35} + m_{36})/2;$$

$$m_{38}^* = m_{39}^* = m_{40}^* = m_{41}^* = (m_{29} + m_{33} + m_{35} + m_{36})/2; \quad m_{42}^* = m_{43}^* = (m_{37} + m_{38} + 2 \cdot m_{39} + m_{40})/2.$$

The coordinates of the equivalent mass points with respect to the fix coordinate system are:

$$
\begin{cases} X_1 = s_1 \\ Y_1 = s_2 \\ Z_1 = q_1 - l_1 \end{cases};
\begin{cases} X_2 = 0 \\ Y_2 = 0 \\ Z_2 = q_1 - l_1 \end{cases};
\begin{cases} X_3 = 0 \\ Y_3 = 0 \\ Z_3 = q_1 \end{cases};
\begin{cases} X_4 = 0 \\ Y_4 = s_3 \\ Z_4 = q_2 - l_2 \end{cases};
\begin{cases} X_5 = 0 \\ Y_5 = 0 \\ Z_5 = q_2 - l_2 \end{cases};
\begin{cases} X_6 = 0 \\ Y_6 = 0 \\ Z_6 = q_2 \end{cases};
\begin{cases} X_8 = l_{11} \cdot \cos(q_3) \\ Y_8 = l_{11} \cdot \sin(q_3) \\ Z_8 = q_1 \end{cases}
$$

$$
\begin{cases} X_7 = \cdot \cos(q_3) \\ Y_7 = l_{11}/2 \cdot \sin(q_3); \\ Z_7 = q_1 \end{cases}
\begin{cases} X_9 = \sqrt{d_1^2 - (q_2 - q_1)^2} \cdot \cos(q_3) \\ Y_9 = \sqrt{d_1^2 - (q_2 - q_1)^2} \cdot \sin(q_3) \\ Z_9 = q_1 \end{cases};
\begin{cases} X_{10} = \left(b_1/2 + \sqrt{d_1^2 - (q_2 - q_1)^2} \right) \cdot \cos(q_3) \\ Y_{10} = \left(b_1/2 + \sqrt{d_1^2 - (q_2 - q_1)^2} \right) \cdot \sin(q_3) \\ Z_{10} = q_1 \end{cases};
$$

$$
\begin{cases} X_{11} = X_{C_1} \\ Y_{11} = Y_{C_1} \\ Z_{11} = q_1 \end{cases};
\begin{cases} X_{12} = \sqrt{(d_1/2)^2 - ((q_2 - q_1)/2)^2} \cdot \cos(q_3) \\ Y_{12} = \sqrt{(d_1/2)^2 - ((q_2 - q_1)/2)^2} \cdot \sin(q_3) \\ Z_{12} = (q_1 + q_2)/2 \end{cases};
\begin{cases} X_{13} = d_{12} \\ Y_{13} = s_2 \\ Z_{13} = q_4 + l_3 \end{cases};
\begin{cases} X_{14} = d_{12} \\ Y_{14} = 0 \\ Z_{14} = q_4 + l_4 \end{cases};
\begin{cases} X_{15} = d_{12} \\ Y_{15} = 0 \\ Z_{15} = q_4 \end{cases};
$$

$$
\begin{cases} X_{16} = d_{12} - s_1 \\ Y_{16} = s_2 \\ Z_{16} = q_5 + l_5 \end{cases};
\begin{cases} X_{17} = d_{12} \\ Y_{17} = 0 \\ Z_{17} = q_5 + l_6 \end{cases};
\begin{cases} X_{18} = d_{12} \\ Y_{18} = 0 \\ Z_{18} = q_5 \end{cases};
\begin{cases} X_{19} = l_{12}/2 \cdot \cos(\alpha) \\ Y_{19} = l_{12}/2 \cdot \sin(\alpha) \\ Z_{19} = q_4 \end{cases};
\begin{cases} X_{20} = l_{12} \cdot \cos(\alpha) \\ Y_{20} = l_{12} \cdot \sin(\alpha) \\ Z_{20} = q_4 \end{cases};
\begin{cases} X_{23} = X_{C_2} \\ Y_{23} = Y_{C_2} \\ Z_{23} = q_4 \end{cases};
$$

$$
\begin{cases} X_{21} = \sqrt{d_2^2 - (q_5 - q_4)^2} \cdot \cos(\alpha) \\ Y_{21} = \sqrt{d_2^2 - (q_5 - q_4)^2} \cdot \sin(\alpha) \\ Z_{21} = q_4 \end{cases};
\begin{cases} X_{22} = \left(b_2/2 + \sqrt{d_2^2 - (q_5 - q_4)^2} \right) \cdot \cos(\alpha) \\ Y_{22} = \left(b_2/2 + \sqrt{d_2^2 - (q_5 - q_4)^2} \right) \cdot \sin(\alpha) \\ Z_{22} = q_4 \end{cases};
\begin{cases} X_{27} = \left(X_{C_1} + X_{C_2} \right)/2 \\ Y_{27} = \left(Y_{C_1} + Y_{C_2} \right)/2 \\ Z_{27} = (q_1 + q_4)/2 \end{cases};
\tag{15}
$$

$$
\begin{cases} X_{24} = \sqrt{(d_2/2)^2 - ((q_5 - q_4)/2)^2} \cdot \cos(\alpha) \\ Y_{24} = \sqrt{(d_2/2)^2 - ((q_5 - q_4)/2)^2} \cdot \sin(\alpha) \\ Z_{24} = (q_5 + q_4)/2 \end{cases};
\begin{cases} X_{25} = X_{C_1} \\ Y_{25} = Y_{C_1} \\ Z_{25} = q_1 - l_7 \end{cases};
\begin{cases} X_{26} = X_{C_1} \\ Y_{26} = Y_{C_1} \\ Z_{26} = q_1 - l_8 \end{cases};
\begin{cases} X_{29} = X_{C_1} + q_6 \cdot \cos(\psi) \cdot \sin(\theta) \\ Y_{29} = Y_{C_1} + q_6 \cdot \sin(\psi) \cdot \sin(\theta) \\ Z_{29} = q_1 - l_8 - q_6 \cdot \cos(\theta) \end{cases};
$$

$$
\begin{cases} X_{30} = i_{\Delta 30}/2 \cdot \cos(q_3) \\ Y_{30} = i_{\Delta 30}/2 \cdot \sin(q_3) \\ Z_{30} = l_{14} \end{cases};
\begin{cases} X_{31} = i_{\Delta 30}/2 \cdot \cos(q_3 + \pi) \\ Y_{31} = i_{\Delta 30}/2 \cdot \sin(q_3 + \pi) \\ Z_{31} = l_{14} \end{cases};
\begin{cases} X_{32} = d_{12} - i_{\Delta 31}/2 \cdot \cos(\alpha) \\ Y_{32} = i_{\Delta 31}/2 \cdot \sin(\alpha) \\ Z_{32} = l_{13} \end{cases};
$$

$$
\begin{cases} X_{33} = d_{12} - i_{\Delta 31}/2 \cdot \cos(\alpha + \pi) \\ Y_{33} = i_{\Delta 31}/2 \cdot \sin(\alpha + \pi) \\ Z_{33} = l_{13} \end{cases};
\begin{cases} X_{34} = s_1 + i_{\Delta 32}/2 \cdot \cos(q_1^*) \\ Y_{34} = s_2 + i_{\Delta 32}/2 \cdot \sin(q_1^*) \\ Z_{34} = l_{14} \end{cases};
\begin{cases} X_{35} = s_1 + i_{\Delta 32}/2 \cdot \cos(q_1^* + \pi) \\ Y_{35} = s_2 + i_{\Delta 32}/2 \cdot \sin(q_1^* + \pi) \\ Z_{35} = l_{14} \end{cases};
$$

$$
\begin{cases} X_{36} = i_{\Delta 33}/2 \cdot \cos(q_2^*) \\ Y_{36} = s_3 + i_{\Delta 33}/2 \cdot \sin(q_2^*) \\ Z_{36} = l_{14} \end{cases};
\begin{cases} X_{37} = i_{\Delta 33}/2 \cdot \cos(q_2^* + \pi) \\ Y_{37} = s_3 + i_{\Delta 33}/2 \cdot \sin(q_2^* + \pi) \\ Z_{37} = l_{14} \end{cases};
\begin{cases} X_{43} = X_{C_1} + i_{\Delta 35}/2 \cdot \cos(q_6^* + \pi) \cdot \sin(\psi) \\ Y_{43} = Y_{C_1} + i_{\Delta 35}/2 \cdot \cos(q_6^* + \pi) \cdot \cos(\psi) \\ Z_{43} = q_1 - l_8 + i_{\Delta 35}/2 \cdot \sin(q_6^* + \pi) \cdot \sin(\theta) \end{cases}
$$

$$\begin{cases} X_{38} = d_{12} + i_{\Delta 33}/2 \cdot \cos\left(q_4^*\right) \\ Y_{38} = s_3 + i_{\Delta 33}/2 \cdot \sin\left(q_4^*\right) \\ Z_{38} = l_{14} \end{cases} ; \begin{cases} X_{39} = d_{12} + i_{\Delta 33}/2 \cdot \cos\left(q_4^* + \pi\right) \\ Y_{39} = s_3 + i_{\Delta 33}/2 \cdot \sin\left(q_4^* + \pi\right) \\ Z_{39} = l_{14} \end{cases} ; \begin{cases} X_{40} = d_{12} - s_1 + i_{\Delta 34}/2 \cdot \cos\left(q_5^*\right) \\ Y_{40} = s_2 + i_{\Delta 34}/2 \cdot \sin\left(q_5^*\right) \\ Z_{40} = l_{14} \end{cases} ;$$

$$\begin{cases} X_{41} = d_{12} - s_1 + i_{\Delta 34}/2 \cdot \cos\left(q_5^* + \pi\right) \\ Y_{41} = s_2 + i_{\Delta 34}/2 \cdot \sin\left(q_5^* + \pi\right) \\ Z_{41} = l_{14} \end{cases} ; \begin{cases} X_{42} = X_{C_1} + i_{\Delta 35}/2 \cdot \cos\left(q_6^*\right) \cdot \sin(\psi) \\ Y_{42} = Y_{C_1} + i_{\Delta 35}/2 \cdot \cos\left(q_6^*\right) \cdot \cos(\psi) \\ Z_{42} = q_1 - l_8 + i_{\Delta 35}/2 \cdot \sin\left(q_6^*\right) \cdot \sin(\theta) \end{cases} .$$
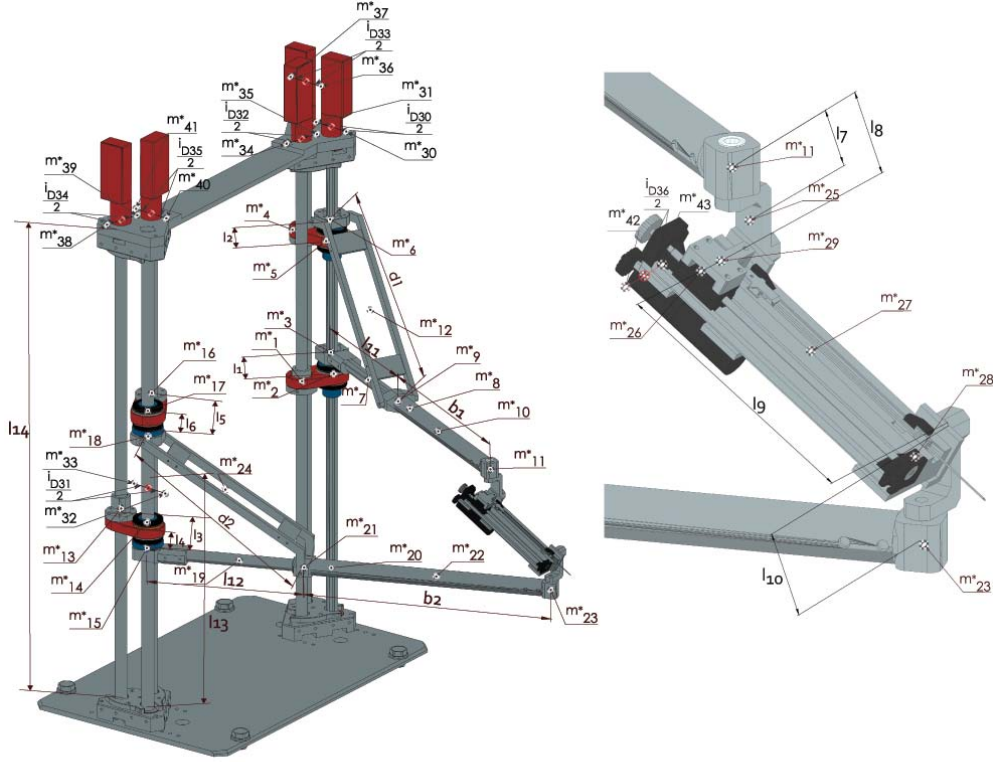

Fig. 4 – The PARA-BRACHYROB lumped masses.

In order to obtain the dynamic model for PARA-BRACHYROB, the virtual work principle has been used:

$$\delta W = \delta q^T \cdot \tau + \sum_{i=1}^{43} \delta X_{Mi}^T \cdot \left(T_i^{In} + T_i^g\right) = 0 , \tag{16}$$

where $\delta q^T \cdot \tau$ is the virtual work of all actuating forces and moments and $\sum_{i=1}^{43} \delta X_i^T \cdot \left(T_i^{In} + T_i^g\right)$ is the virtual work of inertia forces and gravitation forces corresponding to the equivalent system. The matrices of the inertia and gravitational forces are defined as follows:

$$T_i^{In} = -m_{Mass\_i} \cdot \ddot{X}_{Mi} , \quad T_i^g = m_{Mass\_i} \cdot G , \quad T_i = T_i^{In} + T_i^g = -m_{Mass\_i} \cdot \left(\dot{X}_{Mi} - G\right). \tag{17}$$

Considering subsequently each of the mass points M_i defined above, the following relation between the velocity vector of the points and the one of the active joints can be written:

$$\delta X_{M_i} = J_i \cdot \delta q \quad \delta X_{M_i}^T = \delta q^T \cdot J_i^T \tag{18}$$

$$J_i = \begin{bmatrix} \partial X_i/\partial q_1 & \partial X_i/\partial q_2 & \partial X_i/\partial q_3 & \partial X_i/\partial q_4 & \partial X_i/\partial q_5 & \partial X_i/\partial q_6 \\ \partial Y_i/\partial q_1 & \partial Y_i/\partial q_2 & \partial Y_i/\partial q_3 & \partial Y_i/\partial q_4 & \partial Y_i/\partial q_5 & \partial Y_i/\partial q_6 \\ \partial Z_i/\partial q_1 & \partial Z_i/\partial q_2 & \partial Z_i/\partial q_3 & \partial Z_i/\partial q_4 & \partial Z_i/\partial q_5 & \partial Z_i/\partial q_6 \end{bmatrix}, i = 1, \ldots, 43 \tag{19}$$

Subsequently, the equations (18) can be derived with respect to time leading to the expressions which characterize the relation between the equations of the active joints accelerations and the ones of each individual point of concentrated mass:

$$\ddot{X}_I = J_I \cdot \ddot{q} + \dot{J}_i \cdot \dot{q}. \tag{20}$$

From (16), and using the (17) to (20), the torque vector is obtained:

$$\tau = -\sum_{i=0}^{43} J_i^T \cdot \left(T_i^{In} + T_i^g \right). \tag{21}$$

3. SIMULATION RESULTS AND EXPERIMENTAL TESTS

In a real-case scenario of needle placement inside the patient, the robot moves from a starting (arbitrary) position and orientation of the needle (point $S(X_S, Y_S, Z_S)$ and orientation ψ_S and θ_S) up to an insertion point $I(X_I, Y_I, Z_I)$ into the patient's body, position in which the needle is oriented. From this point onward, the needle is inserted into the patient, using only the needle insertion module up to the target point $T(X_T, Y_T, Z_T)$ (inside the tumour).

The analytic algorithm presented in section 1 has been implemented in Matlab using a set of geometric parameters that fit the experimental model designed and presented in figure 1: $b_1 = 395$ mm, $b_2 = 495$ mm, $d_1 = d_2 = 400$ mm, $l_c = 170$ mm, $l_8 = 67$ mm, $d_{12} = 615$ mm. The maximum velocity and acceleration for the needle orientation and position at the insertion point are: $v_{1\max} = 20$ mm$/s$, $a_{1\max} = 10$ mm$/s^2$. During needle insertion, no tissue contact has been considered, leading to a low actuation force in the q_6 active joint. For the proper determination of the resistance force which appears during tissue penetration, a test bench has been developed, modeling a medically relevant scenario. Thus, a calibrated press, model ZWICK/ROEL has been used to insert a BT needle into a large chunk of pork meat. The insertion point was selected in the median region of the meat and driven with a constant speed of 10mm/s. As shown in the graphics, the resulting tissue resistance reaches peaks of 10.5 N, while the maximum mean value is of about 7.9 N. The considered trajectory is a real-case scenario when target point (tumour) is in the liver. The starting position, the insertion point and the considered target point coordinates (in mm and degrees) are: $X_S = 307.5$; $Y_S = 800$; $Z_S = 400$; $\Psi_S = 90°$, $\theta_S = 60°$, $X_I = 350$; $Y_I = 750$; $Z_I = 250$ and $X_T = 355.7194$; $Y_T = 755.0053$; $Z_T = 244.1818$. The data obtained in Matlab, using the Analytical Model (AM) have been compared with the simulation data through a multibody simulation software – RecurDyn from Siemens NX (MBS), where the friction forces have also been neglected. The working parameters used in this paper represent the upper limits for speed and acceleration imposed by the BT procedure, leading to the conclusion that the control algorithm of the robot can be implemented using the simplified inverse dynamic model developed by the authors. Analyzing the simulation plots for these inverse dynamic models, a very good correlation between the two curves is shown, validating the new inverse analytical model developed in this paper (Fig. 5). The maximum error (Err) between the values of the two curves is 5.98% (the error being computed as: Err $= |AM - MBS|/AM \cdot 100$ [%]).
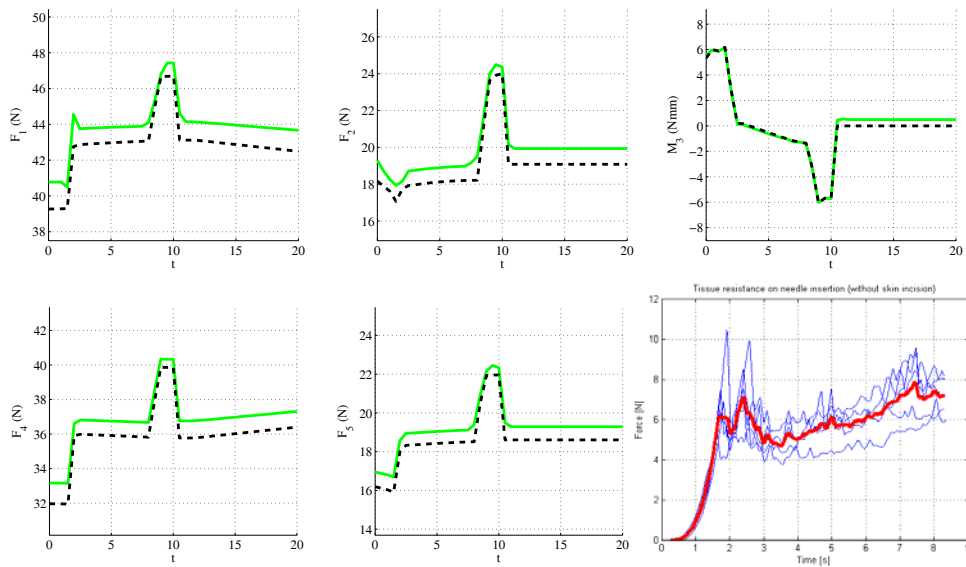
Fig. 5 – Forces and torques comparison between the AM – MATLAB (green, continuous line) and the MBS – RecurDyn (black, dashed line). Experimental tests for the needle insertion (q_6).

4. CONCLUSIONS

The goal of the paper is to develop an easy and fast way to compute the forces/torques of the robot for given laws of motion for the end effector, allowing a better control of the needle position, orientation and insertion. Using the virtual work and the lumped masses principles, the analytical inverse dynamic model has been presented in the paper. The experimental data concerning the needle insertion stage show that special care is needed during the skin penetration where the data shows a force peak which could to needle deflection. Together with an algorithm which will correlate the insertion speed with the resistance force of the tissues, the authors are confident that the robotic system will be able to perform the task with the required accuracy. The developed model has been used to elaborate a MATLAB simulation software on real trajectories and the results have been compared to those obtained by using a multi-body simulation commercial software. The errors introduced by using the lumped masses model are small, proving that this methodology can be applied on a large scale for parallel robots as an alternative to the classical approaches.

ACKNOWLEDGEMENTS

REFERENCES

1. BAUMANN M., *et al*., *Prosper: image and robot-guided prostate brachytherapy*, **32**, *2*, pp. 63–65, 2011.
2. SADJADI, H., HASHTRUDI-ZAAD, K., FICHTINGER, G., *Needle deflection estimation: prostate brachytherapy phantom experiments*, Int. J. Comput. Assist. Radiol. Surg., **9**, *6*, pp. 921–929, 2014.
3. STRASMANN G., *et al*., *Advantage of Robotic Needle Placement on a Prostate Model in HDR Brachytherapy,* Strahlenther Onkol., **187**, *6*, pp. 367–72, 2011.
4. IBRAHIM, O. and KHALIL, W., *Kinematic and dynamic modeling of the 3-RPS parallel manipulator*, 12th IFToMM World Congress, Besançon, 2007.
5. WANG, K. *et al*., *Dynamics Analysis of a Three-DOF Planar Serial-Parallel Mechanism for Active Dynamic Balancing with Respect to a Given Trajectory*, Int. J. Adv. Robotic Sys., **10**, pp. 1–10, 2013.

6. TAGHIRAD, H.D. and NAHON, M.A., *Dynamic Analysis of a Macro–Micro Redundantly Actuated Parallel Manipulator*, Adv. Robotics, **22**, *9*, pp. 949–981, 2012.

7. ABDELLATIF, H. and HEIMANN, B., *Computational efficient inverse dynamics of 6-DOF fully parallel manipulators by using the Lagrangian formalism,* Mechanism and Machine Theory, **44**, *1*, pp. 192–207, 2009.

8. MILLER, K. and CLAVEL, R., *The Lagrange-Based Model of DELTA-4 Robot Dynamics*, Robotersysteme, **8**, pp. 49–54, 1992.

9. STAICU, S. and ZHANG, D., *A novel dynamic modelling approach for parallel mechanisms analysis*, Robotics and Computer-Integrated Manufacturing, **24**, *1*, pp. 167–172, 2008.

10. STAICU, S., *Dynamics of a 2-DOF orienting gear mechanism*, Rev. Roum. Sci. Techn., **5**, *1*, pp. 67–77, 2009.

11. STROE, I., STAICU, S., *Calculus of joint forces using Lagrange equations and principle of virtual work*, Proceedings of the Romanian Academy, Series A, **11**, *3*, pp. 253–260, 2010.

12. CHABLAT, D., WENGER, P., STAICU, S., *Dynamics of the orthoglide parallel robot*, UPB Scientific Bulletin, Series D: Mechanical Engineering, **71**, *3*, pp. 3–16, 2009.

13. PLITEA N., PISLA D., VAIDA C., GHERMAN B. *et al.*, *On the Kinematics of a New Parallel Robot for Brachytherapy*, Proceedings of the Romanian Academy – series A: Mathematics, **15**, *4*, pp. 354–361, 2014.

14. PLITEA N., *et al.*, *Parallel robot for brachytherapy with two kinematic guiding chains of the platform (the needle) type CYL-U*, Patent pending, RO129698-A2, 2013.

15. PISLA D., *et al.*: *Application Oriented Design and Simulation of an Innovative Parallel Robot for Brachytherapy*, Proc. of the ASME 2014 Int. Design Eng. Tech. Conf. and Comp. Inf. Eng. Conf. – IDETC/CIE, 17–20 Aug., New York, USA, 2014.

16. DIZIOGLU, D., *Getriebelehre*, Band 3, Dynamik. Fried Vieweg und Sohn, Braunschweig, 1966.